Simulation study of dual-space microscopy

Darshan B. Desai,* Maksym V. Zhelyeznyakov, Shaima A. S. Alanzi, and Luis Grave de Peralta

Physics Department, Texas Tech University, Lubbock, Texas 79409, USA
*Corresponding author: darshan.desai@ttu.edu

We explore the convergence of the dual-space microscopy (DSM) phase-recovery algorithm. DSM is an optical microscopy technique based on simultaneous observation of an object in the position and momentum spaces. We present one-dimensional (1D) simulations of this technique, demonstrating that the DSM technique is capable to resolve periodic and nonperiodic structures with a resolution well below the Rayleigh resolution limit. Using a simple and faster 1D version of the full 2D DSM algorithm, we simulated the DSM technique for thousands of different samples. Our results demonstrate that the DSM algorithm always converges rapidly to the correct optical disturbance.   © 2016 Optical Society of America

OCIS codes: (110.0180) Microscopy; (100.0100) Image processing.

http://dx.doi.org/10.1364/AO.55.007294

1. INTRODUCTION

The optical disturbance at the real plane (RP) and the Fourier plane (FP) of an optical system can be described by the complex functions $b(x)e^{id(x)}$ and $B(k)e^{iD(k)}$, respectively [1]. Functions $b(x)e^{id(x)}$ and $B(k)e^{iD(k)}$ carry information about the spatial and momentum distribution of the light leaving the object under observation, respectively [1]. Both complex functions carry equivalent information about the object because one can be obtained from the other through a Fourier transform operation [1]. However, optical systems like common optical microscopes and telescopes are often based on detection of the intensity of the light in the system's RP $(b(x)^2)$ [2,3]. Numerous imaging techniques have been developed in order to overcome this limitation; for instance, interferometric synthetic aperture [4–6] and phase-recovery [7–11] imaging techniques have been developed to simultaneously determine amplitude $(b(x))$ and phase $(d(x))$ of the optical disturbance at the RP of the imaging system. Moreover, far-field imaging techniques that are based on the detection of the intensity in the FP of the imaging system $(B(k)^2)$ have also been developed [12–21]. The existence of optical imaging systems based on the detection of $b(x)^2$ and $B(k)^2$ raises general questions about the relative advantages and disadvantages between both imaging approaches. In this work we focus on the lateral resolution limit of optical imaging systems. For instance, it is well known that the resolution limit of a far-field optical microscope that produces wide-field images directly formed in the instrument's RP is the Rayleigh resolution limit $\lambda/(2\,NA_o)$, where λ is the vacuum-wavelength of the light used for imaging, and NA_o is the numerical aperture of the objective lens [1–3]. In contrast, some techniques are capable of producing images with a resolution well below $\lambda/(2\,NA_o)$ [8,11,19,21]. This is related to

recent reports unveiling that a FP image $(B(k)^2)$ may carry more information about objects with a periodical structure than the corresponding RP image $(a(x)^2)$ [22,23]. In this work, using one-dimensional (1D) simulations, we study the convergence of the image reconstruction algorithm of dual-space microscopy (DSM), a recently demonstrated microscope technique based on simultaneous observation of an object in the position and momentum space [24]. DSM is a phase-recovery imaging technique related to Fourier ptychographic microscopy (FPM) [8–11] and ptychographic microscopy (PM) [17–21]. As in PM and FPM, DSM is based on the collection of numerous intensity images using an imaging system with small NA_o; then, as if it was obtained using an imaging system with a large synthetic numerical aperture (NA_s), a high-resolution RP image of the object under observation is obtained by numerical processing the collected intensity images [24]. However, in contrast with PM and FPM, in DSM, pairs of low-resolution RP and FP images are simultaneously collected while illuminating the sample from different directions [24]. As in FPM, but in contrast to PM, the DSM algorithm assumes that the object under observation is illuminated by plane waves in different directions. Hence, DSM can be experimentally realized by adding a second camera for observing the FP of a common optical microscope [22–26]. The resolution limit, λ/NA_s, of the FPM and PM techniques implemented in an optical microscope using an objective lens and a condenser with numeral apertures NA_o and NA_c, respectively, is determined by the achievable $NA_s = NA_o + NA_c$ [11,20,23,27,28]. However, it has been reported that FPM fails to image photonic crystals with a period $\lambda/NA_s < p < \lambda/(2\,NA_o)$ [24,26]. Nevertheless, the capability of the DSM technique for imaging photonic crystals with $\lambda/NA_s < p < \lambda/(2\,NA_o)$ has been

recently experimentally demonstrated [24]. In this work, we studied DSM imaging simulation further for thousands of samples that can be classified in three different groups: (1) photonic crystals with $p > \lambda/(2\,\mathrm{NA}_o)$, (2) photonic crystals with $\lambda/(\mathrm{NA}_o + \mathrm{NA}_c) < p < \lambda/(2\,\mathrm{NA}_o)$, and (3) nonperiodic samples with a mixture of different periodic structures. Using one-dimensional simulations, we first demonstrate that DSM permits us to obtain images with a resolution better than the Rayleigh resolution limit, independently of the object's structure, and then, we present the convergence of the DSM algorithm for a wide range of samples above and below Rayleigh resolution limit. This paper is organized as follows: in Section 2, we describe the DSM phase-recovery algorithm. In Section 3, we describe the process to obtain simulated low-resolution RP images and corresponding FP images with small NA_o from the one-dimensional object, thus mimicking experimental image acquisition. The results of simulations and convergence of the DSM algorithm are presented in Section 4. Finally, the conclusions of this work are presented in Section 5.

2. DUAL-SPACE MICROSCOPY

FPM and PM are supposed to be alternative but equivalent phase-recovery imaging methods due to optics' reciprocity principle [29,30]. This is not surprising since the optical disturbance at the RP and the FP of an optical system carry equivalent information about the object under observation, because one can be obtained from the other through a Fourier transform operation [1]. However, microscope cameras only record the intensity of the light; therefore, the phase of the optical disturbance is lost during the measurement process. Consequently, the information content of RP and FP intensity images about the structure of the sample may not be equivalent. Different information content of RP and FP images occurs when imaging photonic crystals [31] with $\lambda/\mathrm{NA}_s < p < \lambda/(2\,\mathrm{NA}_o)$ [22,23]. A typical example of a pair of RP and FP images with different information content about a photonic crystal is shown in Fig. 1.

RP and FP images that are shown in Figs. 1(a) and 1(b), respectively, were obtained using a microscope with an objective lens with $\mathrm{NA}_o = 0.8$ and ×50 magnification. The $\lambda = 450$ nm illumination source was a light-emitting diode (LED) from a hemispherical digital condenser (HDC) with $\mathrm{NA}_c = 0.97$ [24–26]. The intensity images shown in Fig. 1 are dark-field images since $\mathrm{NA}_c = 0.97 > \mathrm{NA}_o = 0.8$; and consequently, the zero-order diffraction spot is not visible in the FP image shown in Fig. 1(b). The single spot visible in Fig. 1(b) is a first-order diffraction spot associated with the photonic crystal's periodicity $p = 500$ nm. As sketched in Fig. 1(c), knowledge of NA_c and the position in the FP image of the first-order diffraction spot permits us to extract the value of p from the FP image shown in Fig. 1(b) [24–26]. The blue-continuous-line circumference in Fig. 1(c) represents the region of the FP that is observable with the microscope's objective lens. The red-discontinuous-line circumference in Fig. 1(c) was traced requiring that it should pass through the first-order diffraction spot, and has a radius equal to NA_c; then, the distance between the centers of both circumferences is equal to λ/p, which is the distance in numerical aperture units between
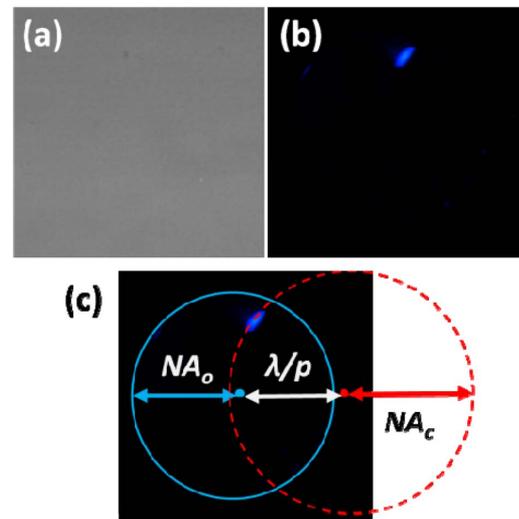
Fig. 1. (a) RP image and (b) FP image of a photonic crystal with periodicity $p = 500$ nm, which were obtained with $\mathrm{NA}_c = 0.97$ and $\mathrm{NA}_o = 0.8$. (c) Construction for obtaining p from the FP image shown in (b). The distance between the centers of the two circumferences is equal to λ/p.

the zero and first diffraction orders. Consequently, the amount of information about the structure of the photonic crystal carried by FP intensity images, like the one shown in Fig. 1(b), should permit their use for obtaining an image of the photonic crystal. PM, which is based on collection of several diffraction patterns, permits to resolve crystals with a period $p_{\min} < p < \lambda/(2\,\mathrm{NA}_o)$ because when $p_{\min} < p < \lambda/(2\,\mathrm{NA}_o)$, all the RP and FP images of a photonic crystal look like the RP and FP images shown in Figs. 1(a) and 1(b), respectively [24,26]. However, FPM is based on the collection of several RP intensity images. The nonzero uniform intensity seen in the RP image shown in Fig. 1(a) is the only information about the photonic crystal structure contained in this intensity RP image. This corresponds to a single bright spot in the FP image. However, the information about the position of the spot in the FP image is not in the intensity RP image but in the phase of the complex light field at the microscope's RP, which is not recorded in the RP camera. This is the reason why, in contrast to PM, FPM cannot resolve photonic crystals with $p < \lambda/(2\,\mathrm{NA}_o)$ [24,26]. DSM was developed as a technique complementing FPM to overcome this shortcoming of FPM [24]. Therefore, as sketched in Fig. 2, the DSM algorithm is related to the FPM phase-recovery algorithm [8–11]. It should be noted that both DSM and Gerchberg–Saxton [12,13] algorithms use RP and FP images, but the DSM algorithm needs a set of RP-FP image pairs obtained with different illumination angles.

As shown in the block (1) in Fig. 2, the DSM algorithm starts, for instance, assuming amplitude $(a_{m=0}(r))$ and phase $(p_{m=0}(r))$ identically equal to one and zero, respectively, as the initial approximation $(m = 0)$ corresponding to the high-resolution RP intensity image $(a_{m=0}(r)^2)$. Then, as shown in the block (2) in Fig. 2, the first actual approximation $(m = 1, j = 1)$ of the amplitude and phase corresponding to
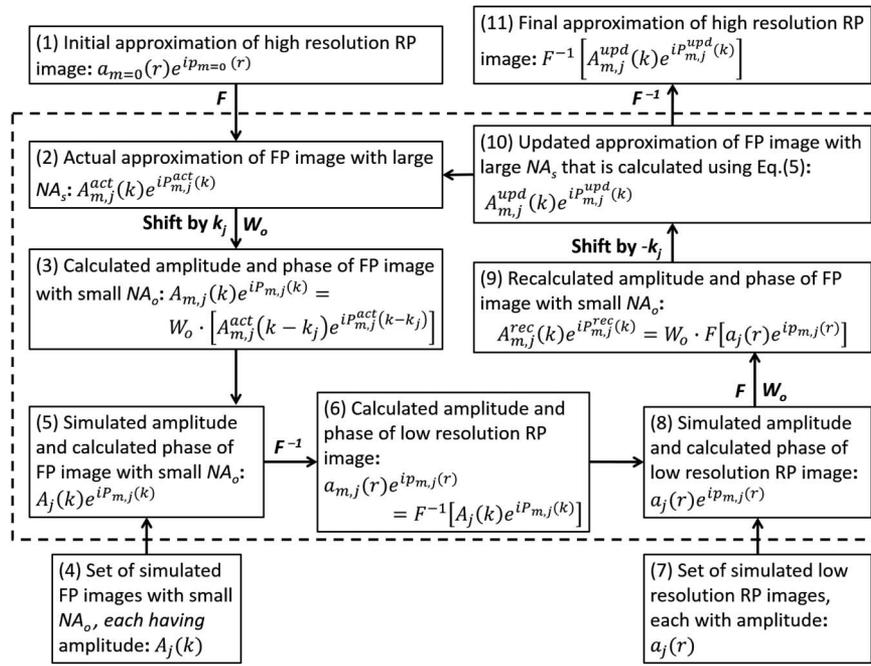
Fig. 2. DSM phase-recovery algorithm. The part of the algorithm included in the box with the discontinuous line is repeated for NA_c corresponding to every LED, which constitutes a complete iteration. The algorithm converges after several iterations.

the FP image with large NA_s are calculated by applying a 2D Fourier transform operation (F):

$$A_{m,j}^{act}(k)e^{iP_{m,j}^{act}(k)} = F[a_{m=0}(r)e^{ip_{m=0}(r)}]. \qquad (1)$$

The DSM technique uses a set of low-resolution RP images and the corresponding set of FP images obtained by illuminating the sample obliquely, each time with a plane wave in the direction $k_j = (2\pi/\lambda)NA_c$. The plane wave can be approximately realized using the LEDs in an HDC [24]. A closer experimental realization of the variable-direction plane wave illumination could be a variable-direction laser beam [32]. As shown in the block (3) in Fig. 2, Eq. (2) is used to calculate the first approximation to the amplitude ($A_{m=1,j=1}(k)$) and phase ($P_{m=1,j=1}(k)$) corresponding to the FP image with small $NA_o (A_{m,j}(k)^2)$ that would be observed by illuminating the sample with the LED number j:

$$A_{m,j}(k)e^{iP_{m,j}(k)} = A_{m,j}^{act}(k-k_j)e^{iP_{m,j}^{act}(k-k_j)} \cdot W_o. \qquad (2)$$

In Eq. (2), $k_j = (2\pi/\lambda)NA_c$, where NA_c takes the value corresponding to the LED number j, and W_o is a circular window with radius NA_o, amplitude equal to one and centered at $k = 0$. At this point, as shown in the blocks (4) and (5) in Fig. 2, the calculated amplitude of the FP image with small $NA_o(A_{m,j}(k))$ is substituted by the amplitude of the corresponding experimental FP image ($A_j(k)$). This step differentiates DSM and FPM algorithms. This is the step in the DSM algorithm where the possible extra-information content in the FP images is incorporated to the FPM algorithm. In the next DSM algorithm's step, as shown in the block (6) in Fig. 2, the amplitude ($a_{m,j}(r)$) and phase ($p_{m,j}(r)$) corresponding to the related low-resolution RP image are calculated by applying a 2D inverse Fourier transform operation (F^{-1}):

$$a_{m,j}(r)e^{ip_{m,j}(r)} = F^{-1}[A_j(k)e^{iP_{m,j}(k)}]. \qquad (3)$$

At this point, as shown in the blocks (7) and (8) in Fig. 2, like in FPM, in DSM, the calculated amplitude of the low-resolution RP image ($a_{m,j}(r)$) is substituted by the amplitude of the corresponding experimental low-resolution RP image ($a_j(r)$). Then, as shown in the block (9) in Fig. 2, the amplitude and phase corresponding to the FP image with NA_o are recalculated using the following equation:

$$A_{m,j}^{rec}(k)e^{iP_{m,j}^{rec}(k)} = F[a_j(r)e^{ip_{m,j}(r)}] \cdot W_o. \qquad (4)$$

Finally, as shown in the block (10) in Fig. 2, the updated approximations of the amplitude and phase corresponding to the synthetic numerical aperture are calculated by, first, shifting the complex functions corresponding to the calculated and recalculated FP images with small NA_o by the amount $-k_j$, and then adding a weighted difference between them to the complex function corresponding to the actual approximations of the synthetic numerical aperture, i.e., using Eq. (5):

$$A_{m,j}^{upd}(k)e^{iP_{m,j}^{upd}(k)} = A_{m,j}^{act}(k)e^{iP_{m,j}^{act}(k)}$$
$$+ \alpha[A_{m,j}^{rec}(k+k_j)e^{iP_{m,j}^{rec}(k+k_j)}$$
$$- \gamma A_{m,j}(k+k_j)e^{iP_{m,j}(k+k_j)}]. \qquad (5)$$

As shown by the arrow between blocks (10) and (2) in Fig. 2, after the initial approximation of the FP image with large NA_s is updated, the amplitude and phase corresponding to the updated FP image with NA_s are used as the actual approximation of them ($j = 2$). The operations included in the box with the discontinuous line in Fig. 2 are successively done for each pair of experimental low-resolution RP image and corresponding FP image with small NA_o (indicated by the subindex j).

This constitutes the first iteration ($m = 1$) in the FPM algorithm, and the algorithm should converge after several iterations. Finally, as shown in the block (11) in Fig. 2, the 2D Fourier transform of the complex function corresponding to the updated FP image with large NA_s gives the amplitude and phase corresponding to the final high-resolution RP image.

The capability of DSM for imaging photonic crystals with $\lambda/NA_s < p < \lambda/(2\,NA_o)$ has been already demonstrated [24], but the convergence of the DSM algorithm needs to be tested for a wide range of samples and experimental conditions. As a first step in this direction, we conducted simulations using a 1D version of the DSM algorithm sketched in Fig. 2. In the 1D simulations, the window W_o is a segment of length $2\,NA_o$, amplitude equal to one, and is centered at $k = 0$. In addition, Fourier transforms are 1D operations, and we consider only the simple case $\alpha = 1$ and $\gamma = 0$ in Eq. (5). Taking advantage of the high speed of the 1D FPM algorithm, we performed 1D simulations of DSM imaging of thousands of samples containing periodic structures with periods above and below of $\lambda/(2\,NA_o)$. Also, taking advantage of the simplicity of the 1D simulations, we discuss some interesting cases in order to gain in physical understanding about the DSM phase-recovery algorithm.

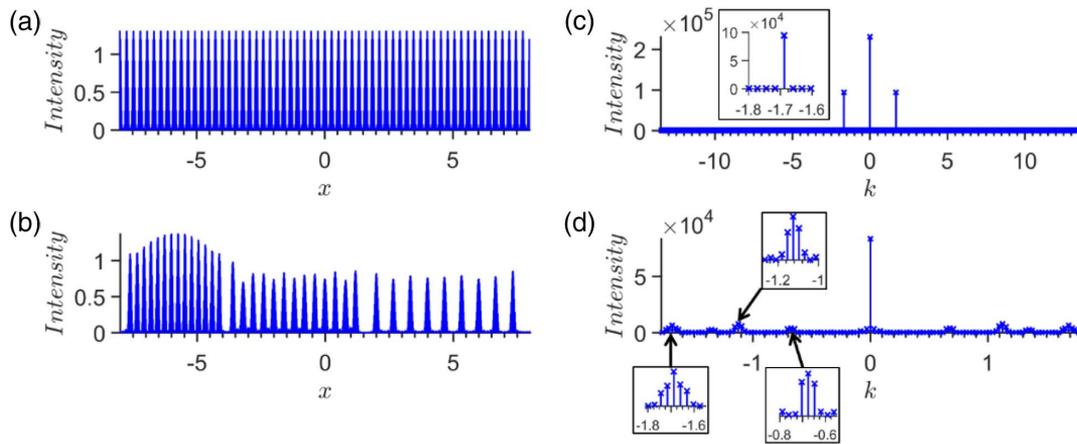## 3. SIMULATION OF LOW-RESOLUTION IMAGES OBTAINED BY ILLUMINATING A ONE-DIMENSIONAL OBJECT FROM SEVERAL DIRECTIONS

Figures 3(a) and 3(b) show the intensity ($a(x)^2$) and phase ($p(x)$), respectively, associated with the light transmitted by a periodic one-dimensional object with $p = 500$ nm that is illuminated by a plane wave impinging the sample at normal incidence [1–3]. Figures 3(c) and 3(d) show the intensity ($A(k)^2$) and phase ($P(k)$), respectively, of the one-dimensional Fourier transform (F) of the complex function $a(x)e^{ip(x)}$; i.e.,

$$A(k)e^{iP(k)} = F[a(x)e^{ip(x)}]. \tag{6}$$

In order to simplify the simulation analysis, in this work, the Fourier transforms are plotted as a function of numerical aperture (NA) units, which can be obtained dividing the wavenumber (k) by $2\pi/\lambda$. We used $\lambda = 450$ nm in our simulations, which matches the emission maximum of common commercial white LEDs [24–26]. Figure 3(c) corresponds to the diffraction pattern that would be produced by illuminating the sample with a plane wave at normal incidence [1–3]. The spikes correspond to diffraction spots of different orders [1–3]. The inclined illumination is provided by a one-dimensional array of LEDs [24–26]. The spots in Fig. 3(c) and its inset correspond
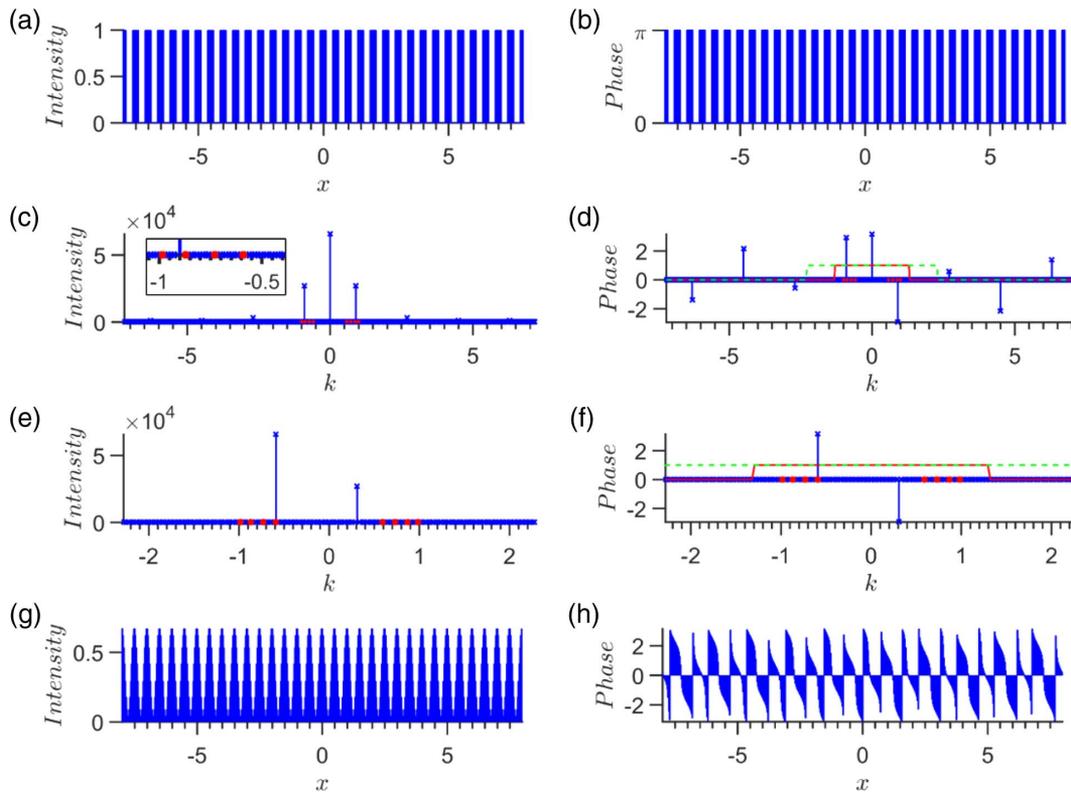
Fig. 3. (a) Intensity and (b) phase associated with light transmitted through a one-dimensional periodic object with $p = 500$ nm illuminated by a plane wave at normal incidence. (c) Intensity and (d) phase corresponding to the Fourier transform of the complex function describing the transmitted light. The small (red) and large (green) windows represent the region of the FP observable by the objective lens and the synthetic numerical aperture, respectively, when the sample is illuminated by perpendicular light. The directions of emission of the LEDs are represented by red spots. (e) Intensity of the FP image and (f) corresponding phase obtained when the object is illuminated in the direction represented by the innermost red spot along $k < 0$. (g) Intensity of the corresponding simulated low-resolution RP image and (h) related phase. Intensity, phase, x, and k are plotted in arbitrary units, radians, micrometers, and NA units, respectively.

Fig. 4. Intensity of (a), (c) high-resolution RP image and (b), (d) corresponding FP images with $NA_s = 1.78$ obtained using the DSM technique and all simulated low-resolution images with $NA_o = 0.8$ corresponding to a 1D object formed by (a), (b) a single periodic structure with $p = 267$ nm and (c), (d) a mixture of structures with three different periods: $p = 267$, 400, and 667 nm. Intensity, x, and k are plotted in arbitrary units, micrometers, and NA units, respectively.

to the illumination direction of four pairs of LEDs with an equivalent condenser numerical aperture of $NA_c = 0.59$, 0.73, 0.87, and 0.98. This distribution of LEDs was chosen to approximately match the distribution of LEDs in reported HDCs [24–26]. The small (red) and large (green) windows in Figs. 3(d) and 3(f) represent the region of the FP observable by the objective lens under perpendicular illumination (W_o) and the synthetic numerical aperture (NA_s) obtainable with the DSM technique, respectively. The minimum superposition between the observable regions of the FP, when the sample is illuminated by adjacent LEDs, was calculated to be 94% and 91% for $NA_o = 1.3$ and 0.8, respectively. Figures 3(e) and 3(f) show an instance of a simulated FP image with small $NA_o(A_j(k)^2)$ and corresponding phase ($P_j(k)$), respectively. This instance corresponds to transmitted light being collected by an objective lens with $NA_o = 1.3$, and the sample being illuminated by the LED with $NA_c = 0.59$, whose corresponding illumination direction is represented by the innermost red spot in the inset of Fig. 3(c). The FP image with small NA_o shown in Fig. 3(e) is the 1D version of the FP image that would be observed experimentally by adding a second camera to an optical microscope, as described in [22–26]. Amplitude and phase corresponding to the FP image with small NA_o related to each LED were calculated using the following equation:

$$A_j(k)e^{iP_j(k)} = A(k - k_j)e^{iP(k-k_j)} \cdot W_o. \qquad (7)$$

Equation (2) corresponds to the successive application of the operations "shift" and "window." First, the complex function $A(k)e^{iP(k)}$ is shifted toward the FP position k_j corresponding to the direction of the illumination produced by the LED number j. The shift is then followed by a multiplication by W_o, so that the resulting FP image is limited to experimentally realizable numerical aperture (NA_o). For instance, after the shift, the zero-order diffraction spike appears in the same position ($NA = -NA_c = -0.59$) as the left innermost green spot in Fig. 3(e). The two diffraction spikes in Fig. 3(e) are the only diffraction spikes that remain inside the window W_o after

shifting the spectrum. The amplitude ($a_j(x)$) and phase ($p_j(x)$) corresponding to the simulated low-resolution RP images ($a_j(x)^2$) are then calculated by the following inverse one-dimensional Fourier transform (F^{-1}):

$$a_j(x)e^{ip_j(x)} = F^{-1}[A_j(k)e^{iP_j(k)}]. \qquad (8)$$

Figures 3(g) and 3(h) show a low-resolution RP image ($a_j(x)^2$) and corresponding phase ($p_j(x)$), which were obtained using Eq. (8) from the simulated FP image and its corresponding phase shown in Figs. 3(e) and 3(f), respectively. A comparison of Figs. 3(a) and 3(g) clearly indicates the low-resolution character of the RP image shown in Fig. 3(g), which has the same periodicity as that of the object, but has lost the sharp corners present in the object shown in Fig. 3(a). The finite numerical aperture of the objective lens limits the maximum spatial frequency that can be collected. Hence, only two spikes, corresponding to the zeroth and first diffraction orders, can be observed in the FP image with small NA_o shown in Fig. 3(e), while numerous spikes are observed in Fig. 3(c). Nevertheless, the observation of the correct periodicity of the sample in the low-resolution RP image shown in Fig. 3(g) means that the sample's periodic structure was resolved. This occurs because $p = 500$ nm $> \lambda/(2 NA_o) = 173$ nm, and p is also larger than the minimum period, $p_{min} = \lambda/(NA_o + NA_c) = 239$ nm, resolvable using bright-field microscopy with maximum inclined illumination corresponding to $NA_c = 0.59 < NA_o$ [22,25,27,28]. The observation of periodic features in the RP image of the sample when two consecutive diffraction orders are captured in the corresponding FP image is in excellent correspondence with the criteria for resolution in the Abbe's theory of image formation, which states that periodic structures in a sample could be observed in the RP image if, and only if, diffraction features corresponding to two consecutive diffraction orders could be observed in the corresponding FP image [22,25,27,28]. All simulated low-resolution RP images and corresponding FP images with small NA_o were obtained following the procedure described in this section.
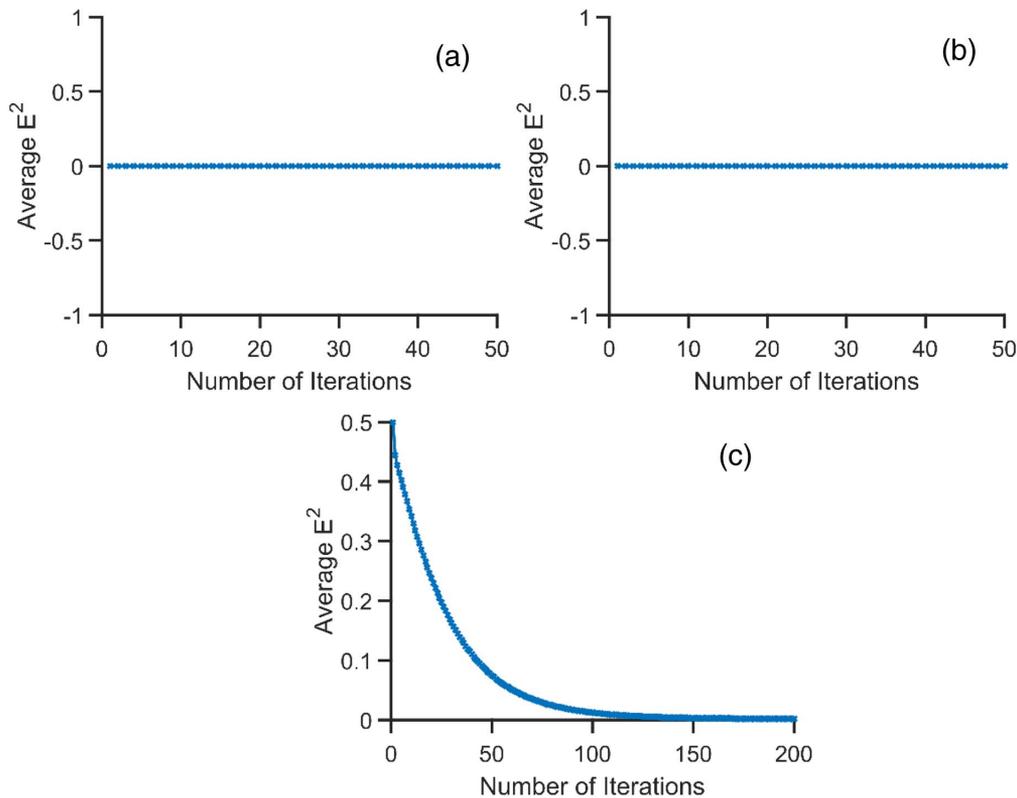
Fig. 5. Plots of the dependence of the average value of the normalized mean-squared error metric on the number of iterations for a 1D object formed by (a), (b) a single periodic structure with (a) $p > \lambda/(2\,\mathrm{NA}_o)$, (b) $\lambda/\mathrm{NA}_s < p < \lambda/(2\,\mathrm{NA}_o)$, and (c) nonperiodic case with a mixture of structures with three different periods: two of them with $p > \lambda/(2\,\mathrm{NA}_o)$, and the other with $\lambda/\mathrm{NA}_s < p < \lambda/(2\,\mathrm{NA}_o)$.

4. IMAGE RECONSTRUCTION WITH DSM ALGORITHM

In order to be sure that we do not miss any important development, we explored the algorithm results up to thousands of iterations, without finding any significant differences from the results obtained at convergence. Figure 4 shows results obtained after 600 iterations of the one-dimensional DSM algorithm using the eight low-resolution RP images simulated with $\mathrm{NA}_o = 0.8$ as described in Section 3.

Figures 4(a) and 4(c) show the high-resolution RP image and the corresponding synthetic FP image with $\mathrm{NA}_s = 1.78$, respectively, which were obtained using all eight simulated low-resolution RP images, the corresponding eight simulated FP images with $\mathrm{NA}_o = 0.8$, and the 1D DSM algorithm. The RP and FP images shown in Figs. 4(a) and 4(c) are position and momentum space intensity images, respectively, of a periodic one-dimensional object with $\lambda/\mathrm{NA}_s \sim 252$ nm $< p = 267$ nm $< \lambda/(2\,\mathrm{NA}_o) \sim 281$ nm. The first-order diffraction spikes located at $\mathrm{NA} = \lambda/267 = 1.6875$ in the inset of Fig. 4(c) indicate that the periodic structure observed in Fig. 4(a) has the correct periodicity $p = 267$ nm. This is in excellent agreement with the experimental results and full 2D DSM simulations previously reported [24], therefore confirming both the validity of our 1D approach to DSM and the capability of the DSM technique for imaging photonic crystal with $\lambda/\mathrm{NA}_s < p < \lambda/(2\,\mathrm{NA}_o)$. Figures 4(b) and 4(d) indicate that DSM, like FPM, can also resolve structures with a period

$\lambda/\mathrm{NA}_s < p < \lambda/(2\,\mathrm{NA}_o)$ in more complex samples. Figures 4(c) and 4(d) show the high-resolution RP image and the corresponding synthetic FP image with $\mathrm{NA}_s = 1.78$, respectively, which were obtained using all eight simulated low-resolution RP images, the corresponding eight simulated FP images with $\mathrm{NA}_o = 0.8$, and the 1D DSM algorithm. The RP and FP images shown in Figs. 4(b) and 4(d) are position and momentum space intensity images, respectively, of a 1D object formed by a mixture of three periodic structures with $p = 267$, 400, and 667 nm. The three periodic structures forming the object can be clearly observed in Fig. 4(c). Moreover, the periods of these structures are correct, as indicated by the first-order diffraction spikes located at $\mathrm{NA} = \lambda/p = 0.675$, 1.125, and 1.6875 in the inset of Fig. 4(d). The results shown in Fig. 4 constitute particular instances indicating that the resolution limit of DSM, like PM, is λ/NA_s; therefore, DSM can resolve periodic structures with $\lambda/\mathrm{NA}_s < p < \lambda/(2\,\mathrm{NA}_o)$ in photonic crystal or in nonperiodic samples. To be sure about the generality of this statement and taking advantage of the high speed of the 1D FPM algorithm, we performed 1D simulations of DSM imaging with $\mathrm{NA}_o = 0.8$ for a large collection of different 1D objects. Figure 5 shows the result of these simulations.

Figures 5(a) and 5(b) show a plot of the dependence of the average value of the normalized mean-squared error metric [33,34] on the number of iterations in the 1D DSM algorithm for photonic crystals with p above and below of $\lambda/(2\,\mathrm{NA}_o)$,

respectively. Two groups with thousand photonic crystals each, and with periods values in the ranges 260 nm $< p <$ 280 nm and 300 nm $< p <$ 600 nm, were used in the generation of the plots shown in Figs. 5(a) and 5(b), respectively. The 1D object corresponding to the plot shown in Fig. 5(c) was a mixture of three different periods similar to the 1D object imaged in Fig. 4(b), where two of these periods were larger than $\lambda/(2\,\mathrm{NA}_o)$, while the third one is in the range 260 nm $< p <$ 280 nm. A value of the normalized mean-squared error metric as defined in [28] (E^2) was calculated in each iteration for each 1D object. As shown in Figs. 5(a) and 5(b), the average value of E^2 is always equal to 0 for photonic crystals; while, as shown in Fig. 5(c), it decreases very rapidly to a value $\sim$0 for more complex samples. The results shown in Fig. 5 clearly support that λ/NA_s is the resolution limit of the DSM technique. In particular, the results shown in Fig. 5(b) corroborate that DSM, in contrast to FPM, can image photonic crystals with $\lambda/\mathrm{NA}_s < p < \lambda/(2\,\mathrm{NA}_o)$.

5. CONCLUSIONS

Using 1D simulations, we have explored the convergence of the DSM phase-recovery algorithm. DSM is an imaging technique based on simultaneous observation of an object in the position and momentum spaces. Presented simulation results are in excellent agreement with recently reported experimental results [24]. In addition, results have demonstrated that DSM is an imaging technique capable to resolve periodic and nonperiodic structures with a resolution well below the Rayleigh resolution limit. Moreover, we have shown that DSM is a novel phase-recovery technique that is able to recover the unmeasured phase of the optical disturbance.

REFERENCES

1. J. W. Goodman, *Introduction to Fourier Optics* (McGraw-Hill, 1968).
2. E. Hecht, *Optics*, 3rd ed. (Addison-Wesley, 1998).
3. M. Born and E. Wolf, *Principles of Optics*, 5th ed. (Pergamon, 1975).
4. T. R. Hillman, T. Gutzler, S. A. Alexandrov, and D. D. Sampson, "High-resolution, wide-field object reconstruction with synthetic aperture Fourier holographic optical microscopy," Opt. Express **17**, 7873–7892 (2009).
5. A. E. Tippie, A. Kumar, and J. R. Fienup, "High-resolution synthetic-aperture digital holography with digital phase and pupil correction," Opt. Express **19**, 12027–12038 (2011).
6. T. Turpin, L. Gesell, J. Lapides, and C. Price, "Theory of the synthetic aperture microscope," Proc. SPIE **2566**, 230–240 (1995).
7. J. R. Fienup, "Phase retrieval algorithms: a comparison," Appl. Opt. **21**, 2758–2769 (1982).
8. G. Zheng, R. Horstmeyer, and C. Yang, "Wide-field, high-resolution Fourier ptychographic microscopy," Nat. Photonics **7**, 739–745 (2013).
9. L. Tian, X. Li, K. Ramchandran, and L. Waller, "Multiplexed coded illumination for Fourier ptychography with LED array microscope," Biomed. Opt. Express **14**, 2376–2389 (2014).
10. K. Guo, S. Dong, P. Nanda, and G. Zheng, "Optimization of sampling pattern and the design of Fourier ptychographic illuminator," Opt. Express **23**, 6171–6180 (2015).
11. X. Ou, R. Horstmeyer, G. Zheng, and C. Yang, "High numerical aperture Fourier ptychography: principle, implementation and characterization," Opt. Express **23**, 3472–3491 (2015).
12. D. Sayre, "Some implications of a theorem due to Shannon," Acta Crystallogr. **5**, 843 (1952).
13. R. W. Gerchberg and W. O. Saxton, "A practical algorithm for determination of phase from image and diffraction plane pictures," Optik **35**, 237–245 (1972).
14. J. R. Fienup, "Reconstruction of an object from the modulus of its Fourier transform," Opt. Lett. **3**, 27–29 (1978).
15. J. W. Miao, P. Charalambous, J. Kirz, and D. Sayre, "Extending the methodology of x-ray crystallography to allow imaging of micrometre-sized non-crystalline specimens," Nature **400**, 342–344 (1999).
16. D. Sayre, "X-ray crystallography: the past and present of the phase problem," Struct. Chem. **13**, 81–96 (2002).
17. H. M. L. Faulkner and J. M. Rodenburg, "Movable aperture lensless transmission microscopy: a novel phase retrieval algorithm," Phys. Rev. Lett. **93**, 023903 (2004).
18. J. M. Rodenburg, A. C. Hurst, A. G. Cullis, B. R. Dobson, F. Pfeiffer, O. Bunk, C. David, K. Jefimovs, and I. Johnson, "Hard-X-ray lensless imaging of extended objects," Phys. Rev. Lett. **98**, 034801 (2007).
19. M. J. Humphry, B. Kraus, A. C. Hurst, A. M. Maiden, and J. M. Rodenburg, "Ptychographic electron microscopy using high-angle dark-field scattering for sub-nanometer resolution imaging," Nat. Commun. **3**, 730 (2012).
20. A. M. Maiden, J. M. Rodenburg, and M. J. Humphry, "Optical ptychography: a practical implementation with useful resolution," Opt. Lett. **35**, 2585–2587 (2010).
21. A. M. Maiden, M. J. Humphry, F. Zhang, and J. M. Rodenburg, "Superresolution imaging via ptychography," J. Opt. Soc. Am. A **28**, 604–612 (2011).
22. D. Dominguez, M. Alhusain, N. Alharbi, A. A. Bernussi, and L. Grave de Peralta, "Fourier plane imaging microscopy," J. Appl. Phys. **116**, 103102 (2014).
23. D. Dominguez, M. Alhusain, N. Alharbi, A. A. Bernussi, and L. Grave de Peralta, "Fourier plane imaging microscopy for detection of plasmonic crystals with periods beyond the optical diffraction limit," Plasmonics **10**, 1337–1344 (2015).
24. D. B. Desai, S. Sen, M. V. Zhelyeznyakov, W. Alenazy, and L. Grave de Peralta, "Super-resolution imaging of photonic crystals using dual-space microscopy," Appl. Opt. **55**, 3929–3934 (2016).
25. S. Sen, L. Molina, D. Cao, D. B. Desai, A. A. Bernussi, and L. Grave de Peralta, "Versatile optical microscopy using a reconfigurable hemispherical digital condenser," Biomed. Opt. Express **6**, 658–667 (2015).
26. S. Sen, D. B. Desai, M. H. Alsubaie, L. Molina, H. Sari-Sarraf, A. A. Bernussi, and L. Grave de Peralta, "Imaging photonic crystals using Fourier plane imaging and Fourier ptychographic microscopy implemented with a computer-controlled hemispherical digital condenser," Opt. Commun. (2016, in review).
27. H. Köheler, "On Abbe's theory of image formation in the microscope," Opt. Acta **28**, 1691–1701 (1981).
28. H. H. Hopkins and P. M. Barham, "The influence of the condenser on microscopic resolution," Proc. Phys. Soc. **63**, 737–744 (1950).
29. J. M. Rodenburg, "Ptychography and related diffractive imaging methods," Adv. Imaging Electron Phys. **150**, 87–184 (2008).
30. R. Horstmeyer and C. Yang, "A phase space model of Fourier ptychographic microscopy," Opt. Express **22**, 338–358 (2014).
31. J. D. Joannopoulos, S. G. Johnson, J. N. Winn, and R. D. Meade, *Photonic Crystals: Molding the Flow of Light* (Princeton University, 2008).
32. C. Kuang, Y. Ma, R. Zhou, J. Lee, G. Barbasathis, R. R. Dasari, Z. Yaqoob, and P. T. So, "Digital micromirror device-based laser-illumination Fourier ptychographic microscopy," Opt. Express **23**, 26999–27010 (2015).
33. J. R. Fienup, "Invariant error metrics for image reconstruction," Appl. Opt. **36**, 8352–8357 (1997).
34. X. Ou, G. Zheng, and C. Yang, "Embedded pupil function recovery for Fourier ptychographic microscopy," Opt. Express **22**, 4960–4972 (2014).